Scientific Research Publishing

Open Journal of Geology, 2025, 15(11), 826-848
https://www.scirp.org/journal/ojg
ISSN Online: 2161-7589
ISSN Print: 2161-7570

Petrographic and Geochemical Characterization of Metaluminous to Peraluminous Granitoids from Goueygoudoum-Fianga (Southwestern Chad): Insights into Magma Sources and Tectonic Setting

Mbaguedje Diondoh[1*], Félix Nenadji Djerossem[2], Gustave Ronang Baïssemia[3], Moussa Ngarena Klamadji[3]

[1]Department of Geosciences, Adam Barka University, Abeché, Chad
[2]Department of Mining, New and Renewable Energies, National Higher Institute of the Sahara and Sahel, Iriba, Chad
[3]Department of Mining and Geological Engineering, Faculty of Life and Earth Sciences, Pala University, Pala, Chad
Email: *sandrinediondoh@gmail.com

How to cite this paper: Diondoh, M., Djerossem, F.N., Baïssemia, G.R. and Klamadji, M.N. (2025) Petrographic and Geochemical Characterization of Metaluminous to Peraluminous Granitoids from Goueygoudoum-Fianga (Southwestern Chad): Insights into Magma Sources and Tectonic Setting. *Open Journal of Geology*, **15**, 826-848.
https://doi.org/10.4236/ojg.2025.1511043

Received: October 10, 2025
Accepted: November 25, 2025
Published: November 28, 2025

Abstract

The Goueygoudoum-Fianga localities, situated within the Central African Orogenic Belt to the east of the Mayo Kebbi massif (Chad), are dominated by various granitoid types: granodiorite, biotite granite (either deformed or undeformed), and microgranite. These intrusive rocks were emplaced within a greenstone belt and are geochemically divided into two major peraluminous series. The first series, classified as I-type, exhibits a weakly potassic calc-alkaline affinity with a ferro-magnesian composition. It is characterized by low concentrations of V, Cr, Co, Ni, Mg#, Nb/U, and Ce/Pb, along with high levels of alkalis and light rare earth elements (LREE), and positive Eu anomalies. These features suggest an origin related to partial melting of the continental crust, typical of volcanic arc settings. However, elevated Br and Sr contents, combined with low ratios (Rb/Sr, La/Sm, and $(Ta/La)_N$, high Rb/Th values, and negative anomalies in Nb, Ta and Ti, point to the influence of a metasomatized mantle. The second series, identified as A-type, is distinguished by high concentrations of SiO_2, K_2O, FeO, and incompatible elements, as well as negative anomalies in Sr, Eu, and Ti. This series is derived from partial melting of metagreywackes, métapelites and metabasic to tonalitic in an intraplate tectonic setting. Its geochemical signature also reflects mantle influence associated with a subduction-related environment. The evolution of these granitoids is predominantly by the fractional crystallization processes, with possible crustal contamination during emplacement.

Keywords

Goueygoudoum-Fianga, Mayo Kebbi Massif, I-A-Type Granitoids, Partial Melting, Fractional Crystallization

1. Introduction

Orogenic belts around the world are predominantly composed of granitoids, which play a crucial role in the transfer of heat and material within the Earth's crust [1]-[3]. Based on the geochemical characteristics of major elements, granitoids are generally classified into three types: peralkaline, metaluminous, and peraluminous [4]-[6]. Peraluminous granitoids are referred to as S-type by [1] [4] [7] and are typically derived from magmas generated by the melting of sedimentary or metasedimentary rocks. According to [8], this genetic classification is less precise when investigating the origin of strongly peraluminous granitoids. He therefore proposed a subdivision of peraluminous granitoids based on A/CNK ratios ($Al_2O_3/(Na_2O + K_2O)$): Weakly peraluminous granitoids (A/CNK = 1.00 - 1.10), containing muscovite and/or biotite in variable proportions; Moderately peraluminous granitoids (A/CNK = 1.10 - 1.20), rich in garnet and muscovite; Strongly peraluminous granitoids (A/CNK = 1.20 - 1.30), containing abundant cordierite and Hyperaluminous granitoids (A/CNK > 1.30), characterized by the presence of aluminosilicates or topaz. In general, S-type peraluminous granitoids may form in various tectonic settings, including: 1) continental collision zones [9]; 2) back-arc extension, subduction of oceanic ridges, and post-collisional phases. S-type granitoids are commonly associated with I-type granitoids, which originate from partial melting of igneous rocks and are typically metaluminous to weakly peraluminous, with lower K/Na ratios than S-type granites [5]. S-type granitoids are as Ta, Nb, Be, Li, and Cs, which are often associated with Sn and/or W deposits [10]. The Precambrian basement of Chad is dominated by I-, S-, and A-type granitoids formed in distinct tectonic settings [11]-[18]. In this paper, we use petrographic and geochemical data from hyperaluminous granitoids of the Goueygoudoum-Fianga area in the Mayo Kebbi region to discuss their origin and tectonic significance.

2. General Geology

The Central African Orogenic Belt (CAOB) in Chad comprises five major Precambrian massifs (**Figure 1(a)**, **Figure 1(b)**): the Tibesti massif in the north, the Ouaddaï in the east, the Guéra in the center, the Baïbokoum in the south and the Mayo Kebbi in the southwest. These geological units are partially overlain by

Phanerozoic formations. The Mayo Kebbi massif, located near the Cameroonian border, represents a significant portion of the CAOB. It lies between the Congo Craton and the Saharan metacraton, resulting from the convergence of the West African, Congo-São Francisco cratons, and the Saharan metacraton during the assembly of West Gondwana ([19] [20] (**Figure 1(a)**, **Figure 1(b)**).

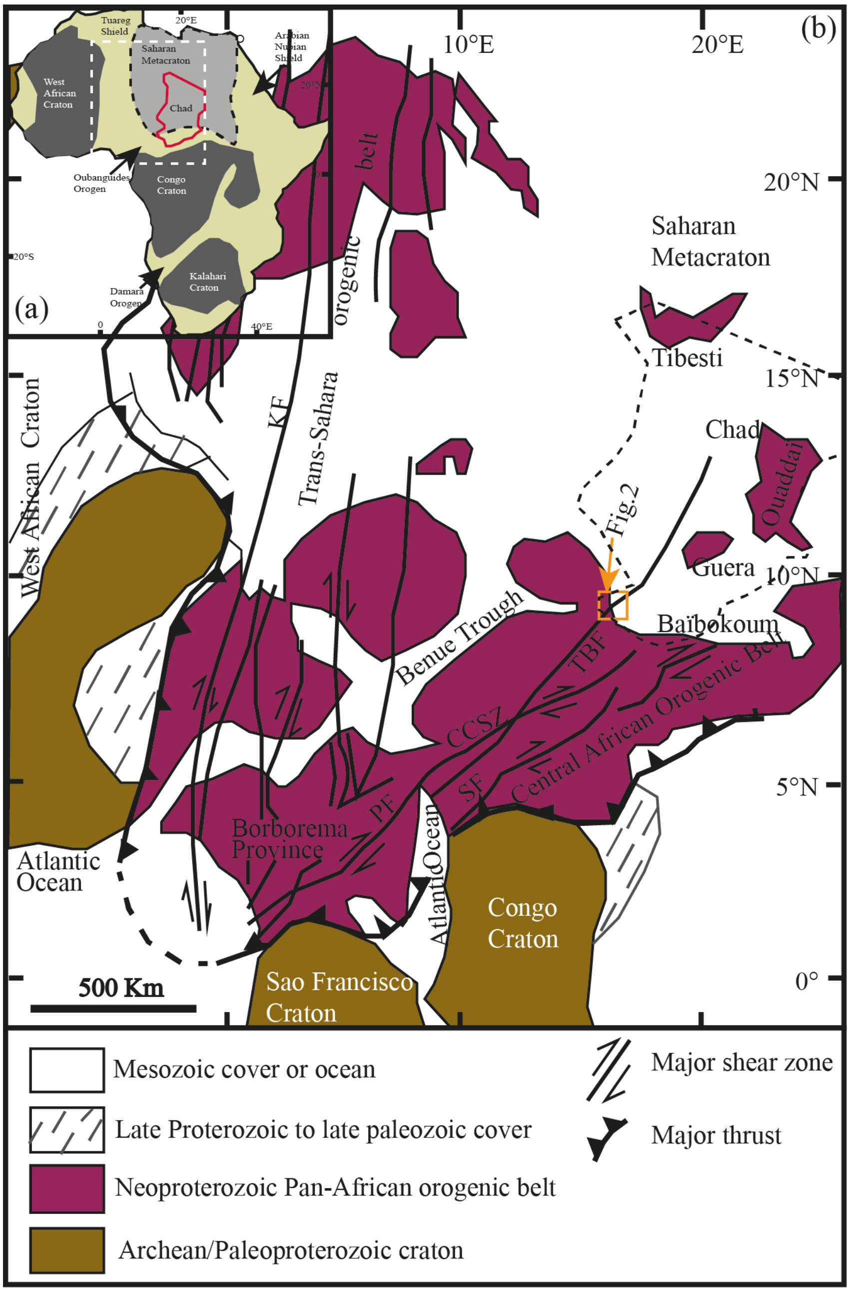

Figure 1. (a) Africa's Precambrian cratons, metacratons and orogenic belts (modified after [22]. (b) Geological sketch map of west-central Africa and northern Brazil with cratonic masses and the Pan-African/Brasiliano provinces of the Pan-Gondwana belt in a Pangea reconstruction; modified from [19] [20]. TBF: Tchollire'-Banyo fault, CCSZ: Central Cameroon shear zone, PF: Pernambuco fault, SF: Sanaga fault, KF: Kandi fault. Dashed outline roughly marks the political boundary of Chad.

The Goueygoudoum-Fianga granitoids are situated within the Mayo Kebbi massif, which is composed of greenstone belts divided into two distinct series (**Figure 2(a)**). The Zalbi Series to the west, forming a SSW-NNE-oriented depression [11], and comprising metagabbros, metabasalts, chlorite schists, talc schists, and serpentinites [11] [21]. **Figure 2(b)** The Goueygoudoum Series to the east, which is poorly exposed and consists of metabasalts associated with metacarbonatites and metacherts.

Felsics to mafic metavolcanic rocks of both series exhibit a tholeiitic geochemical signature, suggesting formation in an island arc or back-arc basin setting. These two series are intruded by the Zalbi granitic pluton, which is mainly composed of coarse-grained biotite-hornblende granite and fine-grained granite. Geochemical analyses indicate an A-type affinity, reflecting crystallization from highly evolved magmas [12]. According to [11], this granite is potassic, peraluminous, and strongly fractionated, associated with post-tectonic intrusions.

U-Pb zircon dating of the biotite–hornblende granites yields a crystallization age of 567 ± 10 Ma, with the presence of older Neoproterozoic xenocrystic zircons (~678 ± 5 Ma) [12]. These granites display εNd values of +7.4, consistent with a depleted mantle source at 570 Ma. [12] propose a genetic model involving: 1) Contribution from juvenile magmas or partial melting of a juvenile basaltic protolith with short crustal residence time; 2) Interaction with older continental materials; 3) Fractional crystallization of biotite granite and 4) Crystallization of feldspars and ferromagnesian minerals.

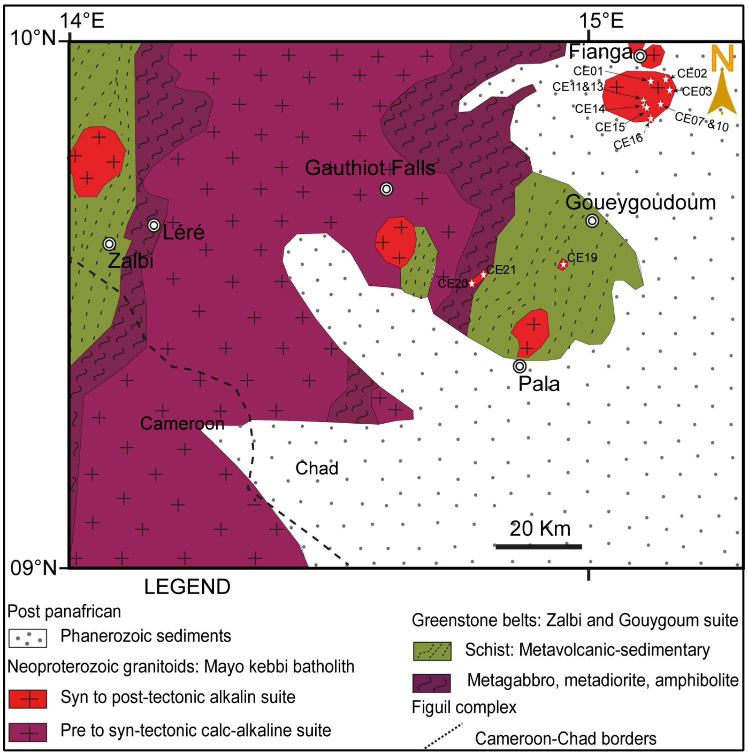

Figure 2. Geological sketch map of the Mayo Kebbi and neighbouring regions. The study area with the position of the samples to be used in the geochemical study.

3. Analytical Methods

Geological field campaigns were conducted in two distinct localities in southern Chad: Goueygoudoum and Fianga. This phase enabled the macroscopic identification of rock facies and the collection of key lithological parameters, including color, texture, mineralogical composition, degree of alteration, and deformation features. A total of thirteen (13) fresh, unaltered samples were selected. These include three samples of deformed granite intruding the green schist series, and ten samples from batholithic bodies partially overlain by cover formations. The latter comprises two granodiorite samples, six biotite granite samples, and two biotite microgranite samples.

Rock samples were sawed into chips for thin section preparation and trimmed to small blocks for geochemical investigations. About 200 to 500 g of each sample was crushed into a steel jaw crusher and then pulverized with an agate ball mill. Powders were digested using an alkali fusion procedure where the powder was mixed to lithium metaborate and melted to produce a glass pellet. The pellet was digested into diluted nitric acid before analyses. Analyses and digestions were made at the ALS Geochemistry-Loughrea (Irland). Prepared samples (0.100 g) are added to lithium metaborate/lithium tetraborate flux, mixed well and fused in a furnace at 1000˚C. The resulting melt is then cooled and dissolved in 100 mL of 4% nitric acid/2% hydrochloric acid. This solution is then analysed by ICP-AES and the results are corrected for spectral inter-element interferences. Oxide concentration is calculated from the determined elemental concentration and the result is reported in that format. The Whole Rock analysis is determined in conjunction with a loss-on-ignition at 1000˚C. The resulting data from both determinations are combined to produce a “total”. For the determination of trace elements, the samples were mixed well and fused in a furnace at 1025˚C. The resulting melt is then cooled and dissolved in an acid mixture containing nitric, hydrochloric and hydrofluoric acids. This solution is then analyzed by ICP-MS.

4. Petrography

4.1. Granodiorite

The granodiorite outcrops as rounded masses and is characterized by a coarse-grained porphyroid texture, displaying feldspar and quartz phenocrysts embedded in a fine-grained matrix composed of ferromagnesian and felsic minerals (**Figure 3(a)**). It is in sharp contact with the biotite microgranite. Under the microscope, the granodiorite exhibits a granular texture and consists of plagioclase, quartz, biotite, and oxides (**Figure 4(a)**, **Figure 4(b)**). Plagioclase (30% - 45%) occurs as subhedral to euhedral crystals, typically in lath-like forms of variable size. Rounded grain edges indicate an advanced degree of alteration. Quartz (20% - 30%) appears as large, elongated grains with lobate margins and neograins, suggesting crystallization under high-temperature conditions. Biotite (10% - 20%) is present as interstitial micrograins or as inclusions within plagioclase and quartz crystals. Opaque minerals (<5%) are observed as subrounded grains, often included within plagioclase and quartz.

4.2. Deformed Biotite Granite

The deformed biotite granite crops out as blocks or slabs, generally weathered, and covers a large area within the study zone (**Figure 3(b)**). It displays a granoblastic texture typical of metamorphosed rocks, with a mineralogical composition dominated by plagioclase, quartz, biotite, and secondary minerals such as chlorite and calcite (**Figure 4(c)**, **Figure 4(d)**). Plagioclase (~60%) forms subhedral to euhedral crystals arranged in laths of varying dimensions and constitutes the dominant phase of the rock. Quartz (10% - 20%) occurs as elongated, interstitial grains between plagioclase crystals, indicating recrystallization under ductile conditions. Biotite (<10%) is generally found as inclusions within plagioclase phenocrysts, suggesting crystallization prior to or synchronous with plagioclase formation. Secondary minerals, including chlorite and calcite, are present in variable amounts and are associated with alteration processes.

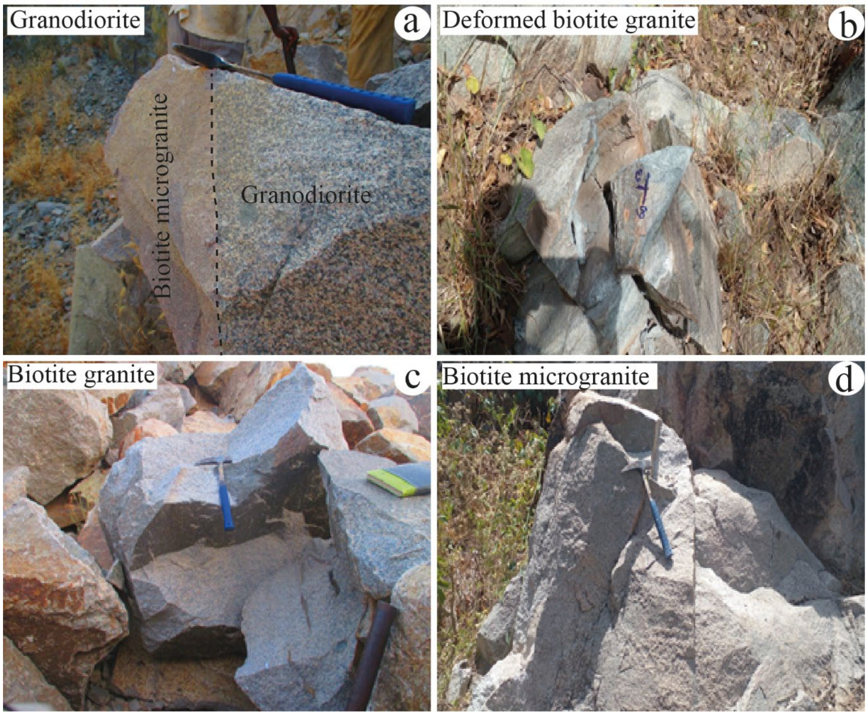

Figure 3. Macroscopic view of granitoids from the Goueygoudoum-Fianga. (a) Granodiorite outcrop in the form of a block, in contact with microgranite; (b) Deformed biotite granite outcrop; (c) Biotite granite outcrop with rounded crystals; (d) Microgranite blocks.

4.3. Biotite Granite

The biotite granite outcrops as rounded masses, blocks, and small hills aligned along a north-south axis (**Figure 3(c)**). It is locally crosscut by dolerite dykes, indicating magmatic events that postdate its emplacement. Thin-section analysis reveals a coarse-grained heterogranular texture, characterized by medium to coarse grains and interlocking phenocrysts (**Figure 4(e)**, **Figure 4(f)**). The primary mineralogical composition includes plagioclase, quartz, and biotite, accompanied by accessory minerals such as zircon, sphene, and opaque minerals. Plagioclase (30% - 40%) occurs as more or less elongated lath-shaped crystals with well-developed polysynthetic twinning, forming the dominant phase of the rock. Quartz (20% - 35%) is present in two distinct generations: the first generation consists of phenocrysts spatially associated with plagioclase, while the second generation comprises neograins arranged in coronas around plagioclase crystals, suggesting late-stage recrystallization. Biotite (10% - 15%) appears as elongated flakes located in the interstices between plagioclase and quartz crystals. Some biotite grains are also observed as inclusions within plagioclase crystals. Accessory minerals (<3%) include zircon, sphene, and opaque phases, typically found as inclusions within the main mineral phases (plagioclase, quartz, biotite), indicating early or synchronous crystallization.

4.4. Biotite Microgranite

Biotite microgranites crop out as north-south trending dykes that crosscut both the granodiorite and the biotite granite (**Figure 3(d)**). These well-defined dykes range in thickness from 10 to 30 cm. They are also found at the summits of certain hills, whose bases consist of rocks with dioritic to granodioritic compositions. The microgranite is distinguished by a fine-grained texture, typical of rapidly cooled facies (**Figure 4(g)**, **Figure 4(h)**). Its mineralogical composition is similar to that of the biotite granite, dominated by plagioclase, quartz, and biotite, along with accessory minerals. Plagioclase (>50%) occurs as euhedral to subhedral lath-shaped crystals, sometimes showing surface alteration, and represents the dominant phase of the rock. Quartz (>20%) is present in two forms: medium-grained interstitial quartz associated with plagioclase, and neograins surrounding plagioclase crystals, indicative of post-magmatic recrystallization. Biotite (<10%) appears as interstitial flakes located between plagioclase and quartz crystals, with some grains also observed as inclusions within plagioclase. Accessory minerals (<3%), including zircon, sphene, and opaque phases, are found as inclusions within the main mineral phases, suggesting early or synchronous crystallization.

5. Geochemistry

5.1. Weathering Index Assessment

To characterize petrogenetic processes in geochemistry, it is essential to evaluate rock weathering, even when samples appear fresh in the field. The Chemical Index of Alteration (CIA), introduced by [23], provides a quantitative measure based on the following molar ratio: CIA = $[Al_2O_3/(Al_2O_3 + CaO^* + Na_2O + K_2O)] \times 100$ (where CaO* represents the concentration of CaO incorporated within the silicate fraction of the rock).

According to [24], three levels of weathering can be distinguished based on CIA values: 1) Intense weathering (feldspar transformation into clay minerals) when CIA > 92; 2) Moderate atmospheric weathering when CIA ranges between 60 and

80 and 3) Low or negligible weathering when CIA < 60. All analyzed granitoid samples exhibit CIA values below 60, indicating minimal to no alteration. This interpretation is further supported by their position within the unweathered rock domain of the CN-K-A ternary diagram (**Figure 5**).

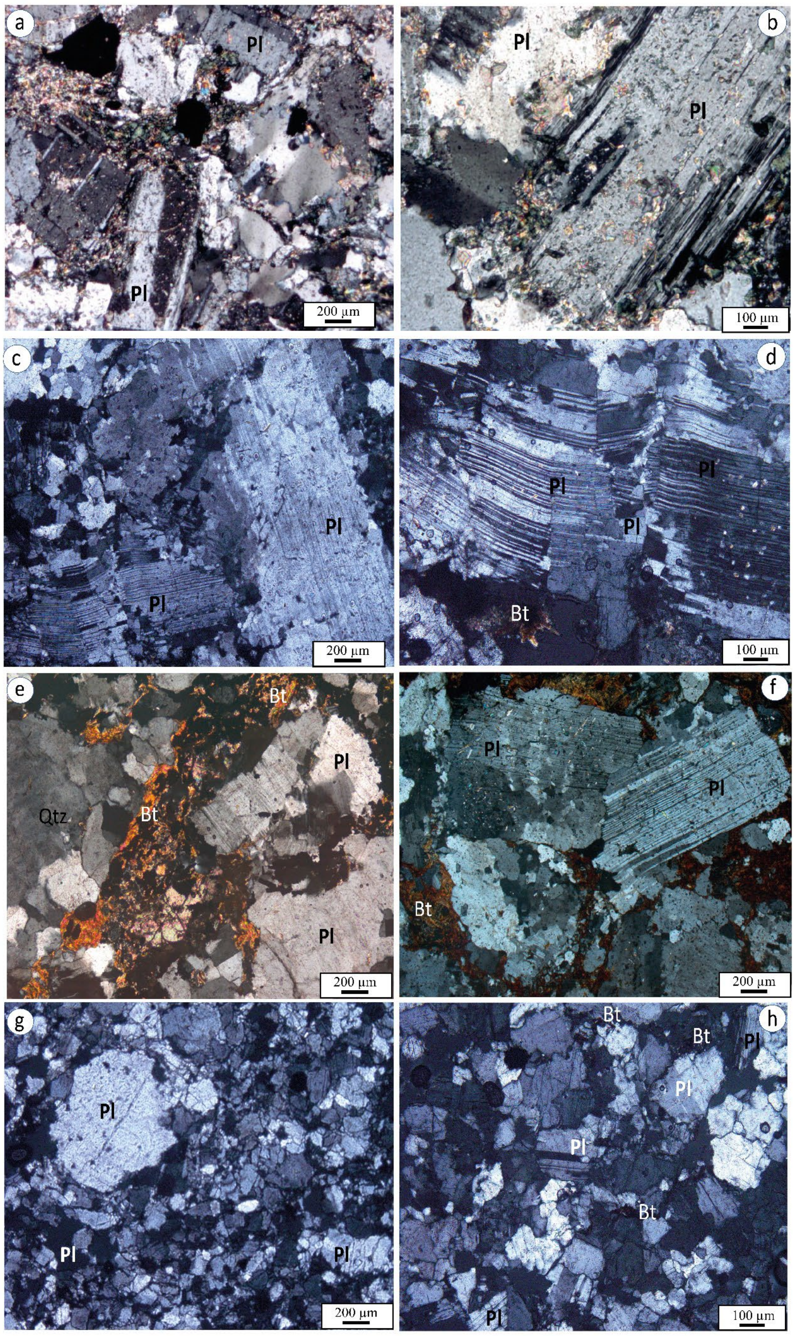

Figure 4. Microscopic view and composition of granitoids (Granodiorite and Deformed biotite granite) from the Goueygoudoum-Fianga. (a) and (b) Granodiorite with a granular structure containing plagioclase crystals of varying sizes; (c) and (d) Deformed biotite granite. (e) and (f) Biotite granite; (g) and (h) biotite microgranite with a microgranular structure. *Bt*: *biotite*; *Pl*: *plagioclase*, *Qtz*: *quartz*, *Bt*: *biotite*; *Pl*: *plagioclase*.

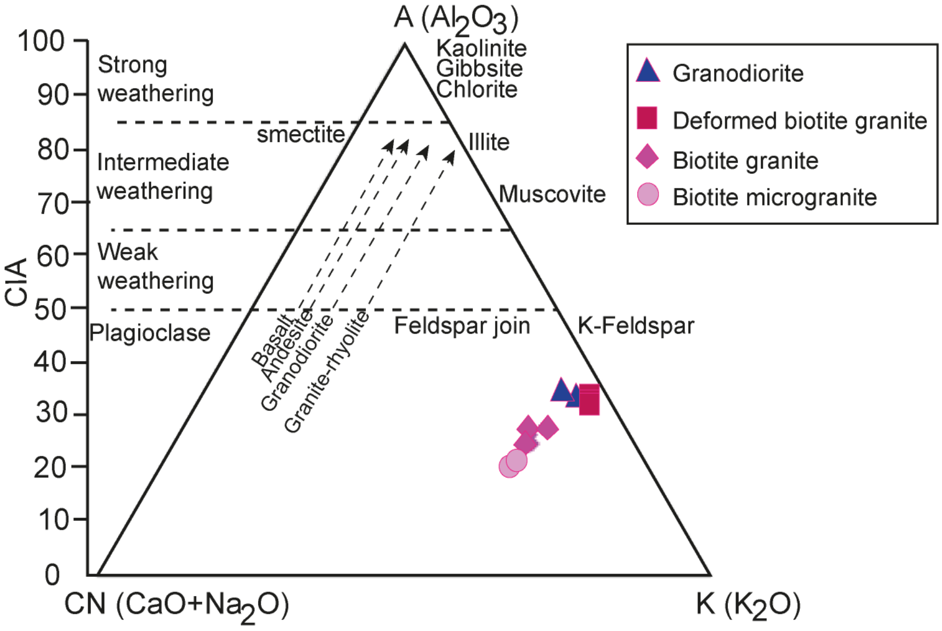

Figure 5. Diagrammes CN-K-A et CIA de [25] appliqués aux granitoïdes de Goueygoudoum-Fianga.

5.2. Major Elements

Geochemical analyses were conducted on 13 representative samples, including 2 granodiorites, 3 deformed biotite granites, 6 biotite granites, and 2 biotite microgranites. Major element concentrations for these granitoids are presented in Table 1 and are characterized by Loss on Ignition (LOI) values ranging from 0.33 to 1.78 wt.%. These granitoids are predominantly intermediate to acidic rocks, with SiO_2 contents ranging from 67.2 to 78 wt.%. TiO_2, P_2O_5, MnO, and CaO values are relatively low across all samples. K_2O concentrations are slightly lower in granodiorites (1.29 - 1.80 wt.%) and deformed biotite granites (0.86 - 1.02 wt.%) compared to biotite granites (2.86 - 3.75 wt.%) and biotite microgranites (4.37 - 4.76 wt.%). Al_2O_3 and Na_2O contents are slightly higher in granodiorites and deformed biotite granites (14.8 - 19 wt.% and 5.62 - 7.54 wt.%, respectively) than in biotite granites and microgranites (11.8 - 13.2 wt.% and 3.95 - 4.32 wt.%). Total alkali contents range from 6.74 to 8.74 wt.%, with K_2O/Na_2O ratios between 0.13 and 1.20, and very low Mg# values (6.43 - 39.27).

In the [26] classification diagram for plutonic rocks (Figure 6(a)), the samples plot within the granodiorite and granite fields, corresponding to subalkaline domains. In the A/CNK vs A/NK diagram [27], the analyzed granitoids are metaluminous and fall within the I-type granitoids field for the granodiorite, biotite granite and biotite microgranite (Figure 6(b)). Deformed biotite granite is peraluminous and fall winthin the I-type granitoids field. They are characterized by K_2O/Na_2O ratios ranging from 0.13 to 1.20, consistent with strongly potassic calc-alkaline granitoids for the granodiorites, biotite granites, and biotite microgranites (Figure 6(c)). The deformed biotite granites are weakly potassic.

According to the [28] classification diagram, the Goueygoudoum-Fianga granitoids exhibit calcic to calc-alkaline affinities (**Figure 6(d)**). In the Harker-type diagram (**Figure 7**), oxide concentrations show two trends with increasing SiO_2 content: a negative correlation for Al_2O_3, TiO_2, Fe_2O_3, MgO, CaO, Na_2O, and P_2O_5, and a positive correlation for K_2O. In both cases, the deformed biotite granites are slightly offset from the other granitoid types.

Table 1. Major (wt%) and trace elements compositions (in ppm) for the Goueygoudoum-Fianga granitoïds.

	Granodiorites		Deformed biotite granites			Biotite granites						Biotite micrograinites	
Samples	CE01	CE15	CE19	CE20	CE21	CE11	CE13	CE02	CE03	CE07	CE16	CE10	CE14
SiO_2	67.20	68.10	70.20	74.40	73.50	73.40	75.70	77.00	77.70	74.90	76.10	78.00	77.20
Al_2O_3	15.25	14.80	19.00	15.45	15.75	13.20	12.00	11.90	11.80	11.80	12.00	12.25	12.40
Fe_2O_3	5.06	4.32	0.37	0.75	1.30	2.77	2.27	2.31	1.96	2.29	2.13	1.16	1.04
MnO	0.14	0.11	0.01	0.01	0.03	0.06	0.05	0.05	0.04	0.05	0.05	0.04	0.02
MgO	1.20	1.40	0.06	0.09	0.34	0.63	0.26	0.13	0.09	0.27	0.26	0.04	0.04
CaO	2.25	3.12	2.73	2.24	2.15	2.03	1.06	0.81	0.63	1.32	1.10	0.29	0.55
Na_2O	6.26	5.62	7.54	5.88	5.90	4.25	4.04	4.24	4.32	4.17	4.09	4.37	3.95
K_2O	1.29	1.80	1.02	0.86	0.94	2.86	3.45	3.57	3.75	3.35	3.48	4.37	4.76
P_2O_5	0.16	0.12	0.01	0.02	0.04	0.05	0.01	0.01	0.01	0.03	0.03	0.01	0.01
LOI	1.78	0.82	0.74	0.73	0.99	1.08	0.75	0.62	0.33	1.03	0.58	0.40	0.36
Total	100.59	100.21	101.68	100.43	100.94	100.33	99.59	100.64	100.63	99.21	99.82	100.93	100.33
Mg#	5.20	4.80	5.10	2.60	4.40	4.10	4.20	4.10	3.90	4.10	4.40	6.40	3.70
FeOt	4.56	3.89	0.33	0.68	1.17	2.50	2.05	2.08	1.77	2.06	1.92	1.05	0.94
A/NK	2.02	1.99	2.22	2.29	2.30	1.86	1.60	1.52	1.46	1.57	1.59	1.40	1.42
A/CNK	1.56	1.40	1.68	1.72	1.75	1.44	1.40	1.38	1.36	1.33	1.38	1.36	1.34
Sc	11.80	11.00	1.90	2.30	3.40	6.30	5.00	5.80	4.00	4.70	5.20	1.90	2.60
V	74.00	77.00	<5	7.00	13.00	26.00	13.00	8.00	<5	14.00	17.00	<5	<5
Cr	147.00	112.00	95.00	200.00	156.00	153.00	150.00	233.00	166.00	171.00	125.00	194.00	172.00
Co	4.00	5.00	<1	<1	1.00	3.00	2.00	1.00	<1	1.00	1.00	1.00	<1
Ni	6.00	9.00	<1	1.00	1.00	4.00	2.00	2.00	1.00	2.00	2.00	1.00	<1
Cu	248.00	262.00	7.00	2.00	2.00	13.00	3.00	3.00	6.00	12.00	3.00	2.00	8.00
Zn	179.00	155.00	10.00	14.00	43.00	96.00	112.00	118.00	123.00	105.00	108.00	76.00	32.00
Rb	34.40	109.50	8.00	7.60	12.30	65.20	76.40	70.50	80.80	56.50	81.20	245.00	116.50
Sr	126.00	109.50	704.00	555.00	629.00	121.50	71.90	61.10	44.80	80.90	68.70	7.10	21.00

Continued

Zr	191.00	192.00	39.00	53.00	67.00	238.00	262.00	286.00	288.00	254.00	257.00	121.00	102.00
Nb	18.05	10.60	0.29	0.65	1.40	12.65	17.65	16.55	19.30	16.55	17.35	53.20	13.80
Cs	0.76	4.28	0.13	0.26	0.29	1.46	2.30	1.66	1.62	2.95	2.89	4.85	1.95
Ba	364.00	262.00	385.00	496.00	413.00	667.00	795.00	988.00	859.00	849.00	797.00	44.50	213.00
Y	159.00	56.10	2.30	2.90	3.30	75.20	96.10	97.50	110.00	84.90	86.40	103.00	66.60
La	27.70	27.30	3.80	1.60	4.70	31.50	36.40	40.30	40.30	35.50	37.40	16.40	17.80
Ce	52.30	49.80	6.20	2.80	10.20	71.00	87.60	92.80	95.90	82.40	86.90	44.00	37.40
Pr	10.05	7.85	0.92	0.39	1.26	9.38	10.90	12.25	12.60	10.80	11.35	5.95	5.35
Nd	48.10	32.80	3.70	1.70	5.60	41.30	47.80	53.90	56.10	47.30	48.90	23.90	22.60
Sm	13.45	7.78	0.78	0.33	1.18	10.25	12.35	13.85	14.30	12.35	12.55	6.64	6.09
Eu	2.85	1.86	0.34	0.26	0.36	1.53	1.86	2.21	2.14	1.81	1.92	0.13	0.28
Gd	18.65	8.40	0.58	0.40	0.88	12.25	14.10	15.35	16.30	13.90	13.60	8.23	7.24
Tb	3.27	1.44	0.08	0.08	0.12	2.18	2.50	2.64	2.90	2.35	2.38	1.78	1.38
Dy	22.10	9.14	0.42	0.44	0.65	13.10	16.05	16.85	18.50	15.40	15.05	12.90	9.38
Ho	4.92	1.88	0.08	0.09	0.11	2.71	3.35	3.45	3.85	2.99	3.08	2.94	2.05
Er	15.10	5.58	0.24	0.28	0.27	8.04	10.50	10.40	11.85	9.49	9.62	10.95	6.73
Tm	2.30	0.90	0.04	0.06	0.04	1.17	1.62	1.59	1.79	1.45	1.46	2.10	1.14
Yb	13.25	5.81	0.21	0.36	0.24	7.43	10.40	9.71	11.40	9.09	9.34	16.10	7.69
Lu	2.16	0.92	0.04	0.06	0.03	1.16	1.60	1.52	1.78	1.44	1.52	2.76	1.30
Hf	6.24	5.71	1.20	1.57	2.06	7.80	9.14	9.83	10.40	9.16	9.41	10.90	5.35
Ta	1.40	0.80	0.10	0.10	0.10	0.80	1.20	1.10	1.20	1.20	1.20	5.20	1.50
W	1.40	1.40	1.20	0.50	0.70	1.30	1.40	1.20	1.00	0.80	1.50	1.60	3.00
Pb	9.00	11.00	5.00	5.00	5.00	13.00	12.00	11.00	10.00	13.00	12.00	23.00	13.00
Th	4.82	6.06	0.18	0.08	0.24	5.68	6.74	5.94	6.84	6.19	7.45	22.20	11.55
U	1.94	2.36	0.14	0.05	0.06	1.40	1.58	1.71	2.02	2.26	2.49	9.27	3.79
$(La/Yb)_N$	2.04	1.33	0.28	0.52	0.51	1.18	1.33	1.84	2.14	2.26	1.28	0.08	0.09
$(Gd/Yb)_N$	10.79	3.99	0.20	0.56	0.39	6.18	7.50	8.67	11.85	11.86	6.41	6.84	2.24
$(La/Sm)_N$	0.61	0.85	1.86	0.75	1.82	0.78	0.77	0.82	0.77	0.80	0.83	0.51	0.65
Eu/Eu*	0.55	0.71	1.55	2.19	1.08	0.42	0.43	0.46	0.43	0.42	0.45	0.05	0.13

5.3. Trace Elements

The Goueygoudoum-Fianga granitoids are characterized by elevated concentrations of barium (Ba), ranging from 44.5 to 859 ppm. Strontium (Sr) values are moderately high in granodiorites and deformed biotite granites (109.5 - 704 ppm), compared to lower concentrations in biotite granites and biotite microgranites (7.1 - 121.5 ppm). Rubidium (Rb) concentrations are high in granodiorites (34 - 109.5 ppm) and biotite microgranites (116.5 - 245 ppm), while they remain low in deformed biotite granites and biotite granites (8 - 81.2 ppm).

In the chondrite-normalized rare earth element (REE) diagram [32] (**Figure 8**), all granitoid samples exhibit parallel REE patterns with enrichment in light rare earth elements (LREE) ($(La/Yb)_N$ = 1.09 - 11.80) relative to middle and heavy rare earth elements (MREE and HREE) ($(Gd/Yb)_N$ = 0.42 - 3.03). Granodiorites (Eu/Eu* = 0.55 - 0.70), biotite granites (Eu/Eu* = 0.41 - 0.46), and biotite microgranites (Eu/Eu* = 0.05 - 0.13) display negative europium anomalies, whereas deformed biotite granites show positive Eu anomalies (Eu/Eu* = 1.08 - 2.18).

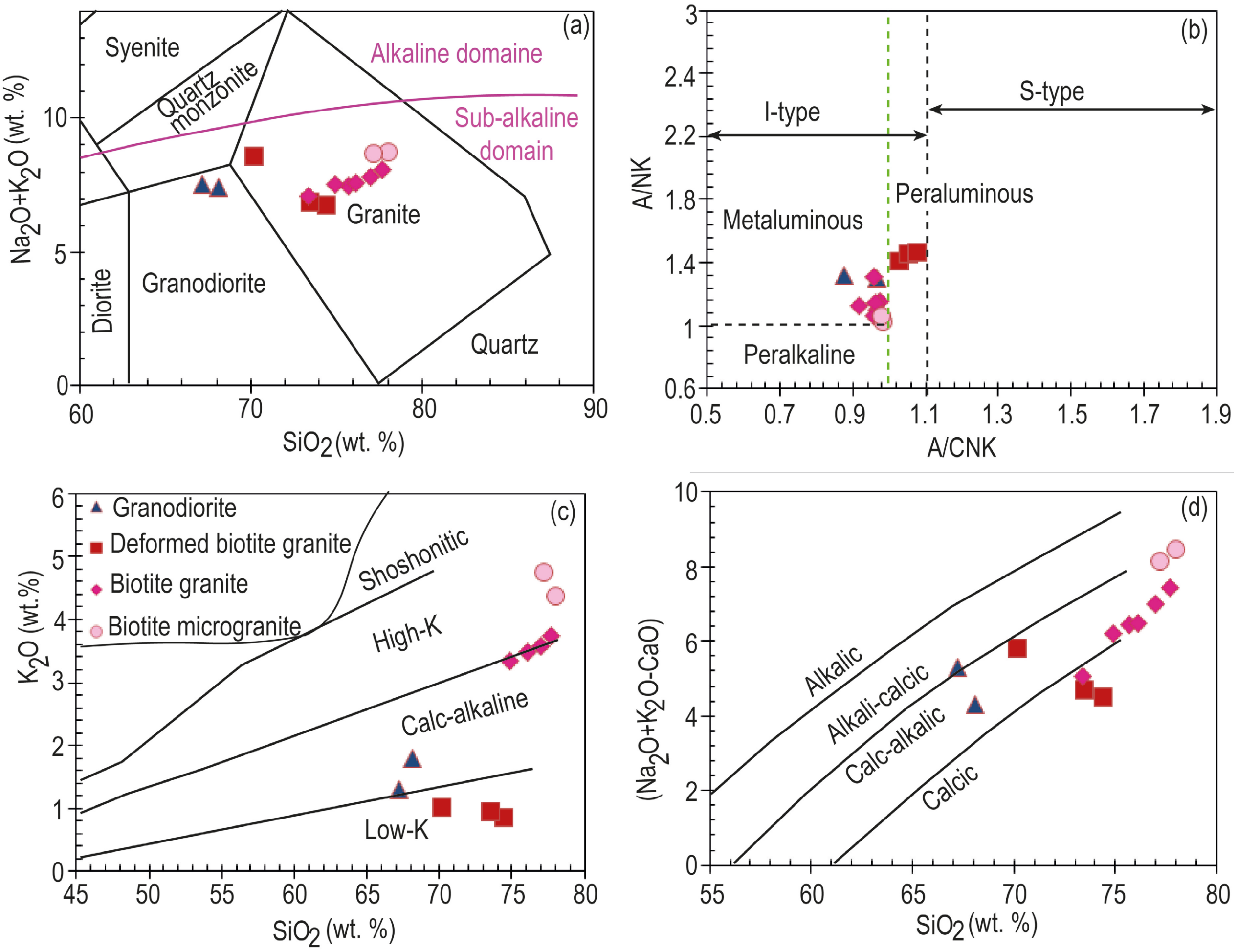

Figure 6. Classification geochemical classification of Goueygoudoum-Fianga granitoids: (a) SiO_2 vs. $Na_2O + K_2O$ diagram of [26]; (b) SiO_2 vs. K_2O diagram of [29]; (c) A/NK = $Al_2O_3/(Na_2O + K_2O)$ vs. A/CNK = $Al_2O_3/(CaO + Na_2O + K_2O)$ after [30]. Dashed line represents boundary between I- and S-type granites [27]; (c) K_2O vs. SiO_2 diagram illustrating the low and high-K calc-alkaline affinities after [26] [31]; (d) SiO_2 vs. $Na_2O + K_2O - CaO$ diagram of [28].

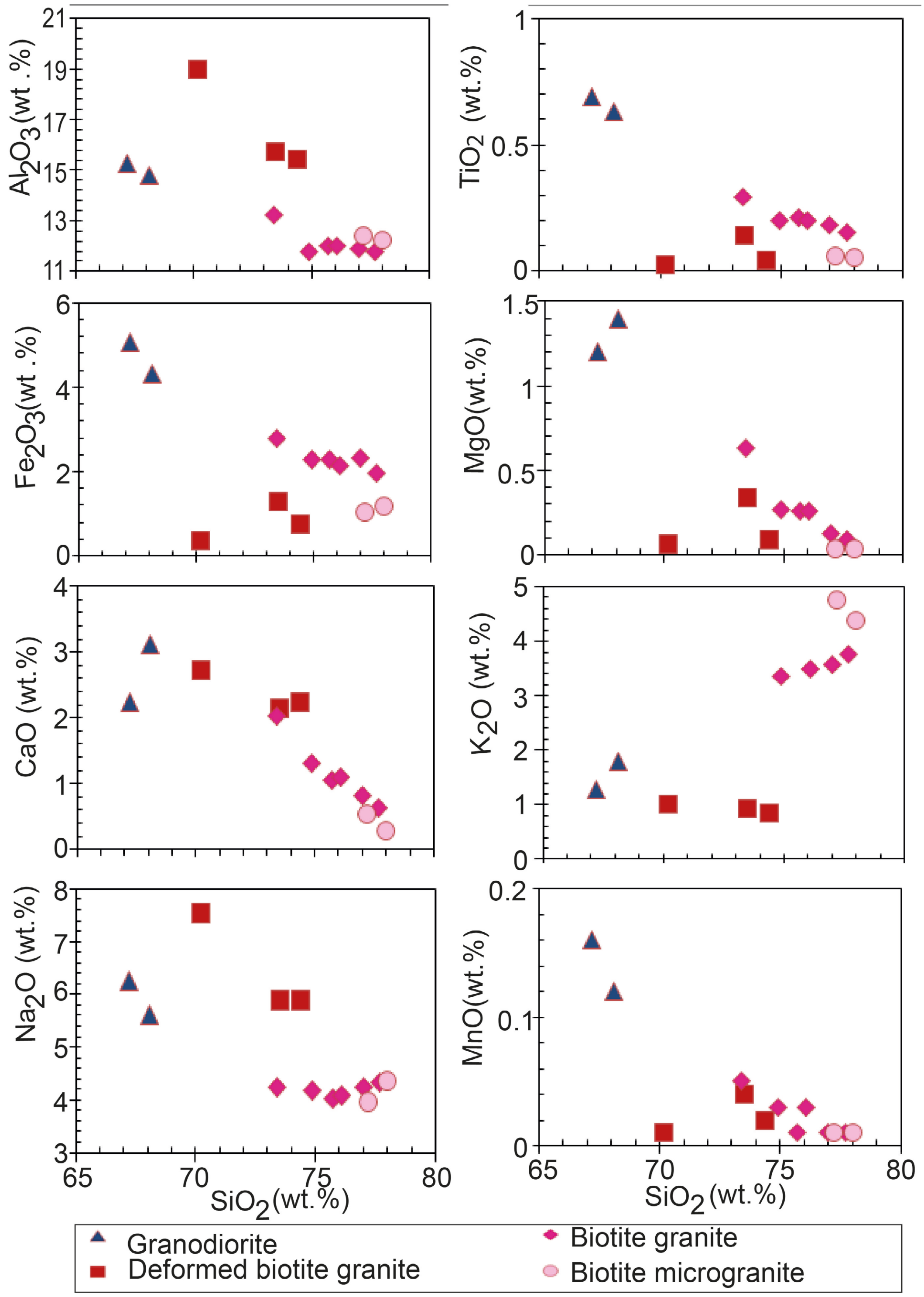

Figure 7. Distribution of Goueygoudoum-Fianga granitoids in the Harker diagram (SiO_2 vs. oxides).

In the primitive mantle-normalized multi-element diagram [32] (**Figure 9**), the Goueygoudoum-Fianga granitoids exhibit negative anomalies in Nb, Sr, Ti, Ta, Eu, Tb, and Ba. Positive anomalies are also observed in Ba, Pb, Sr, Zr, Y, and Th.

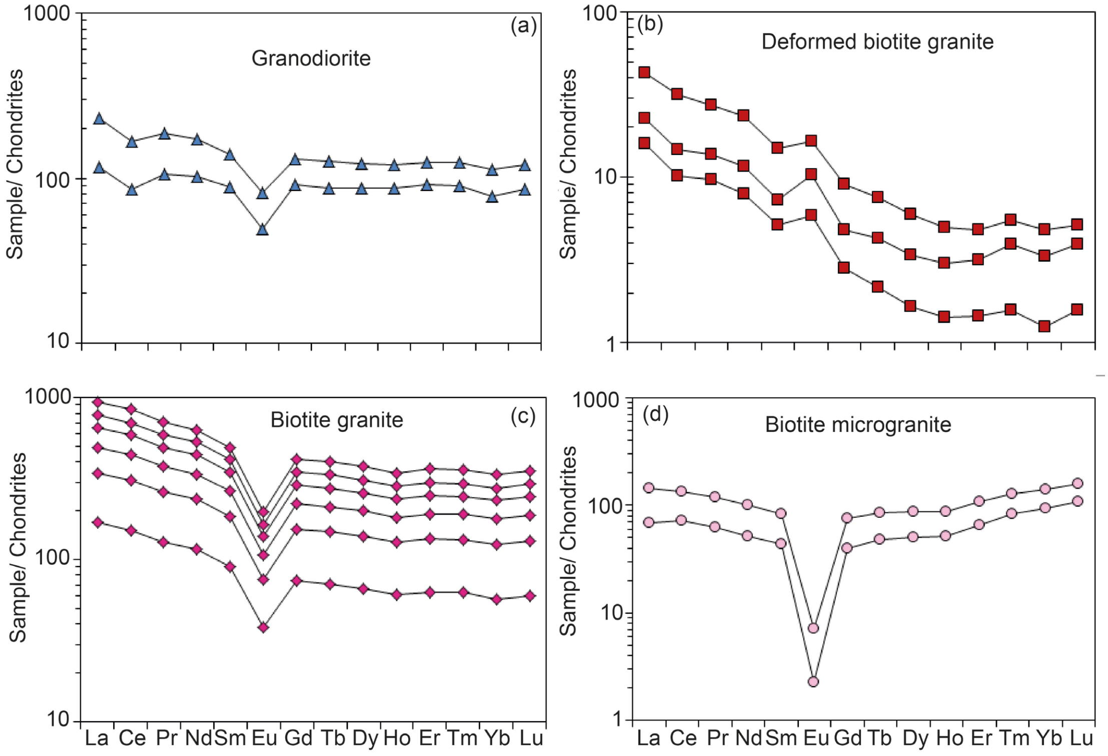

Figure 8. Chondrite-normalized REE patterns of Goueygoudoum-Fianga granitoids. Normalized factors are after [32].

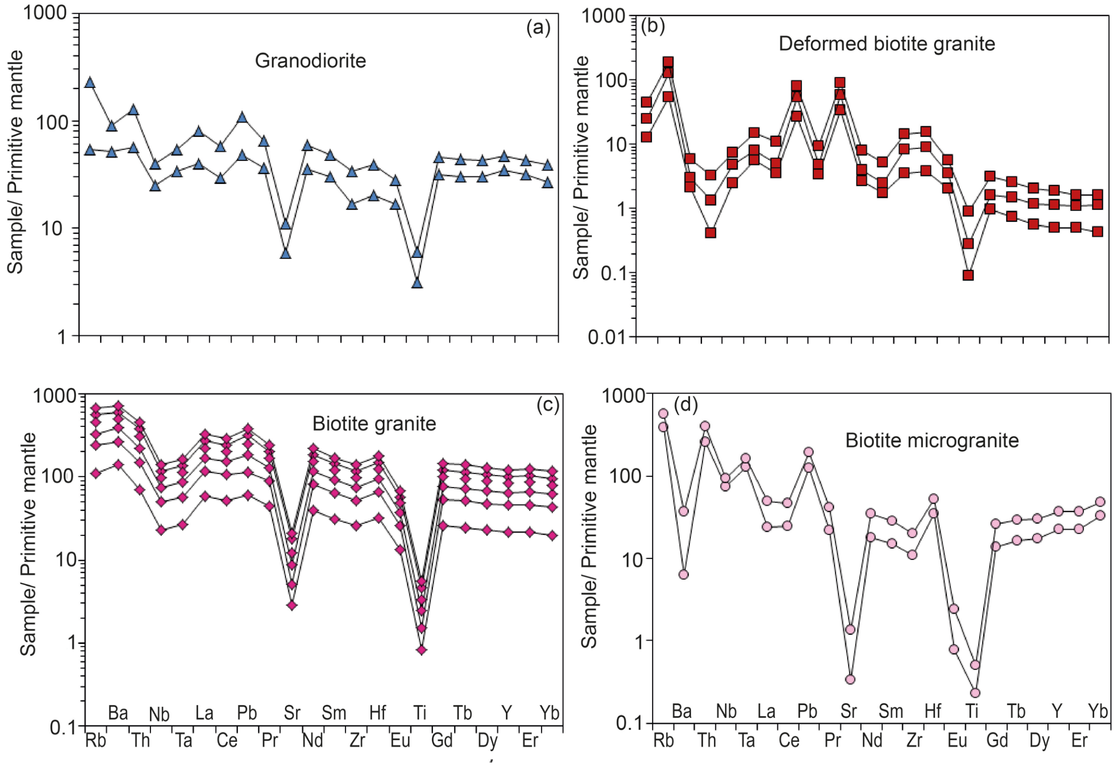

Figure 9. Primitive-mantle-normalized trace element spider diagrams of Goueygoudoum-Fianga granitoids. Normalized factors are after [32].

6. Discussion

6.1. Characterization and Classification

Petrographic and geochemical characteristics of major and trace elements indicate that the Goueygoudoum-Fianga granitoids are primarily composed of granodiorite, deformed biotite granite, biotite granite, and biotite microgranite. These rocks are generally ferroan and peraluminous, displaying a weakly to high-K calc-alkaline nature, predominantly of I-type affinity. However, the granitoids also exhibit high concentrations of SiO_2, K_2O, $Na_2O + K_2O$, FeO, Ga/Al ratios, and high field strength elements (HFSEs), along with low contents of CaO, MgO, P_2O_5, and Al_2O_3, and negative anomalies in Sr, Eu, and Ti. These geochemical signatures are consistent with A-type granites as described in the literature [28] [33] [34]. In the Zr vs. 10000*Ga/Al diagram (**Figure 10(a)**, **Figure 10(b)**), granodiorites, biotite granites, and biotite microgranites plot within the A-type granite field. This classification is consistent with that proposed by [12] for the Mayo Kebbi massif, emplaced at 567 ± 10 Ma under very high temperatures (ranging from 744 ˚C to 923 ˚C), suggesting a highly differentiated magma. Similar granite types were also identified by [35] in the Guéra massif, where they were dated at 554 ± 8 Ma and 546 ± 8 Ma, respectively.

In contrast, the deformed biotite granites correspond to I-type granitoids, as indicated by their molar ratio $Al_2O_3/(CaO + Na_2O + K_2O) > 1.1$. These characteristics are complemented by high concentrations of incompatible elements such as Rb, Ba, and Sr, which are typical of pre-collisional arc-type granites. These rocks were dated at 668 ± 8 Ma by [36], implying a significant contribution from an older basement in their genesis.

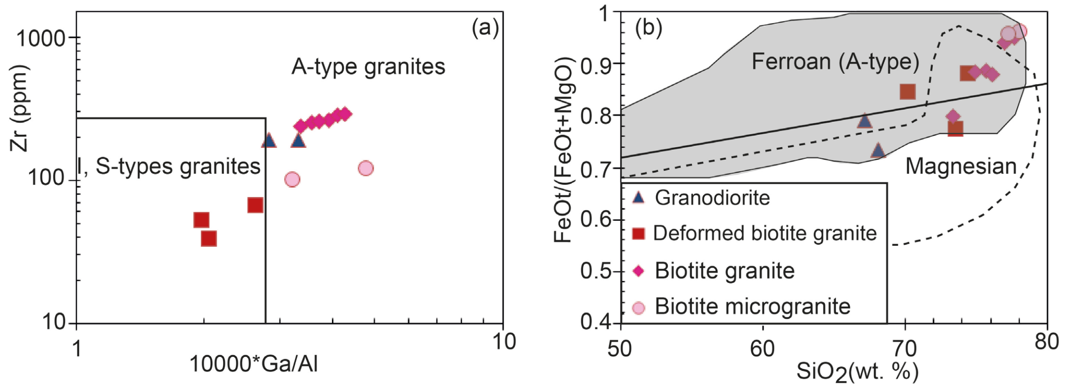

Figure 10. Discrimination plots for the Goueygoudoum granitoids. (a) 10,000*Ga/Al vs. Zr [37]; (b) SiO_2 vs. FeOt/(FeOt + MgO) diagram of after [28].

6.2. Magmatic Evolution Processes of the Goueygoudoum-Fianga Granitoids

This section uses major, trace, and rare earth element concentrations to discuss magmatic evolution processes such as fractional crystallization and crustal contamination/assimilation.

I-type granitoids composed of deformed biotite granite exhibit decreasing concentrations of Al_2O_3, CaO, Na_2O, and K_2O as SiO_2 content increases. These correlations likely reflect fractional crystallization of plagioclase, feldspars, and apatite. In contrast, concentrations of TiO_2, Fe_2O_3, MgO, and P_2O_5 are highly scattered and variations in immobile element ratios such as Zr/Nb and La/Yb suggest an origin linked to partial melting [38]. This geochemical behavior highlights heterogeneity among the deformed biotite granites, possibly resulting from complex partial melting processes or an atypical magmatic source. I-type granites (deformed biotite granites) span both lower continental crust (LCC) and upper continental crust (UCC) domains, as shown in the CN-K-A diagram (**Figure 11(c)**). This trend is also evident in the Rb/Th vs. Rb diagram (**Figure 11(d)**), where deformed biotite granites display signs of crustal contamination.

A-type granitoids reveals linear negative trends for Al_2O_3, CaO, Na_2O, TiO_2, Fe_2O_3, MgO, and P_2O_5, and a positive trend for K_2O in the Harker-type diagrams. According to [39], these correlations play a significant role in mineral phase crystallization. The low CaO content suggests plagioclase and apatite fractionation. Amphibole fractionation accounts for the low MgO levels. Depletion in TiO_2 and P_2O_5 reflects the fractionation of ilmenite and apatite, respectively, while low Fe_2O_3 concentrations are linked to magnetite fractionation.

Overall, the negative oxide trends with increasing SiO_2 content, as described by [40], support fractional crystallization of plagioclase and magnetite. Negative anomalies in Eu, Nb, Ta, and Ti, along with positive anomalies in Eu and Sr, further indicate the fractionation of minerals such as plagioclase, hornblende, biotite, apatite, allanite, and titanite.

Immobile element ratios such as Zr/Nb and La/Yb typically remain constant during fractional crystallization but tend to increase with higher degrees of partial melting [38] [41]. In this study, these ratios remain stable in granodiorites, biotite granites, and fine-grained microgranites (**Figure 11(a)**, **Figure 11(b)**), reflecting a fractional crystallization process. Additionally, the analyzed A-type granitoids exhibit low MgO contents and particularly low Mg# values. Cr, Ni, and Co concentrations are also low. These parameters, well below those of the primitive mantle, indicate an advanced stage of magmatic differentiation, typical of fractional crystallization with or without crustal contamination [42].

Crustal contamination is clearly illustrated in the Nb/U vs. Nb diagram [43] (**Figure 11(c)**), where the granitoids plot within a field indicative of upper continental crust composition, especially for A-type granites. This is also observed in the Rb/Th vs. Rb diagram, where the granodiorites, biotite granites, and fine-grained granites fall within a field likely affected by fractional crystallization with crustal assimilation (**Figure 11(d)**).

6.3. Magma Source and Tectonic Setting of the Goueygoudoum-Fianga Granitoids

I-type granitoids, particularly the deformed biotite granite, exhibit trace element concentrations such as V = 5 - 15 ppm, Cr = 95 - 200 ppm, Co ≤ 1 ppm, Ni ≤ 1 ppm, Mg# = 19.31 - 34.29, Nb/U = 2.07 - 23.33, and Ce/Pb = 0.56 - 2.04. These values are significantly lower than those typical of mantle-derived magmas (V = 151 ppm; Cr = 151 ppm; Co = 94 ppm; Ni = 81 ppm; Mg# = 60; Nb/U = 30; Ce/Pb = 10.2 [40] [45], indicating a dominantly crustal geochemical signature. The Ta/U ratio (0.71 - 2) is also lower than or equal to mantle values, suggesting a mixed origin. These granites are further distinguished by enrichments in Br and Sr, low Rb/Sr ratios, high concentrations of large-ion lithophile elements (LILE), and light rare earth elements (LREE), along with negative anomalies in Nb, Ta, and Ti. Elevated Rb/Th ratios, low La/Sm and $(Ta/La)_N$ ratios, and high alkali contents reinforce this interpretation.

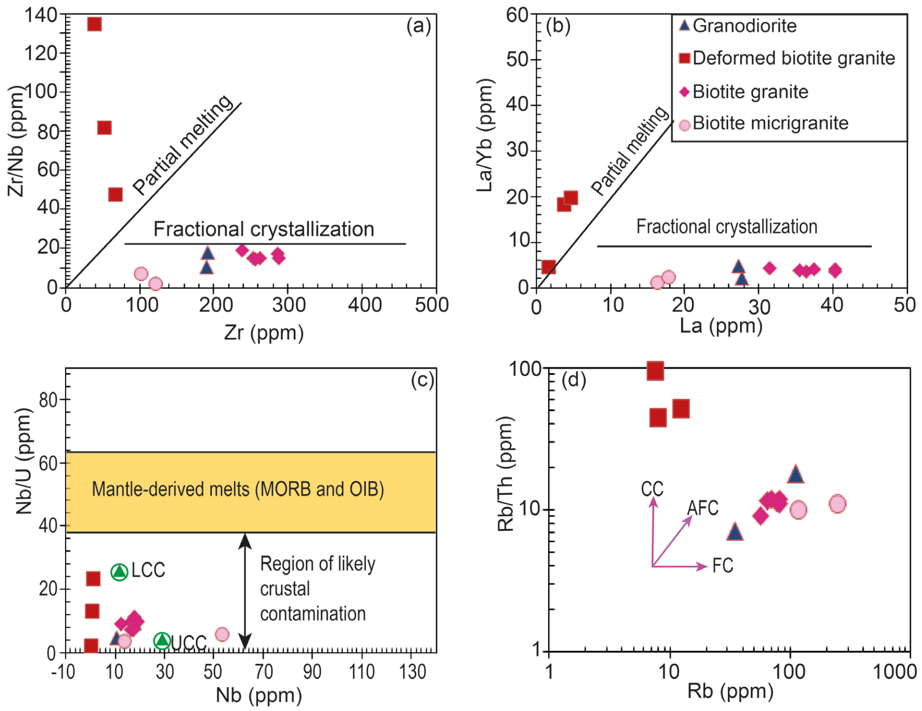

Figure 11. Discrimination of magmatic differentiation process: (a) Zr vs. Zr/Nb; (b) La vs. La/Yb [38] [41]; (c) Nb vs. Nb/U [43]; (d) Rb vs. Rb/Th [44]. CC = Crustal Contamination, AFC = Assimilation Fractional Crystallization; FC = Fracional Crystallization.

According to [46], these geochemical signatures suggest that the parental magma may have originated from partial melting of a metasomatized mantle, combined with crustal contamination. This hypothesis supports a magma mixing model involving mantle-derived melts and crustal inputs. On discriminant diagrams such as Hf–Nb/4–Rb/30, Rb vs. Y + Nb, and $(Nb/Zr)_N$ vs. Zr (**Figure 11(b)**, **Figure 11(c)**), the deformed biotite granites plot within the volcanic arc granite field. Moreover, La/Ta (16 - 38), La/Nb (2.46 - 13.10), and Nb/Ta (2.9 - 14) ratios, along with low Rb contents, reflect a subduction-related genesis [47]. This interpretation is supported by the Zr vs $(Nb/Zr)_N$ diagram, which highlights geochemical signatures indicative of partial melting. (**Figure 11(d)**). Similar granitoid sources have been identified in the Central African orogenic belt, notably in the

Guéra massif [16] [18].

A-type granitoids, including granodiorites, biotite granites, and fine-grained granites, show trace element concentrations of V = 5 - 77 ppm, Cr = 112 - 233 ppm, Co = 1 - 5 ppm, Ni = 1 - 9 ppm, and Mg# = 6.43 - 39.27. These values are also lower than those of mantle-derived magmas, indicating a crustal origin. This is further supported by low Ta/U (0.33 - 0.76), Nb/U (3.64 - 11.17), and Ce/Pb (1.91 - 9.59) ratios, compared to mantle values (Ta/U = 1.1 - 1.8; Nb/U = 30; Ce/Pb = 10.2 [40].

According to [48], the molar ratio diagram of CaO/(MgO + FeOt) vs. Al_2O_3/(MgO + FeOt) helps identify source rocks formed under varying melting conditions. The distribution of Goueygoudoum-Fianga granitoids in this diagram (**Figure 12(a)**) indicates derivation from partial melting of metagreywackes and metapelites, consistent with a crustal source. Similar sources have been reported in the Ouaddaï massif [15], Baïbokoum [17] and Mayo Kebbi [11] [12] [49]. Granodiorite indicates derivation from partial melting of metabasic and tonalitic sources.

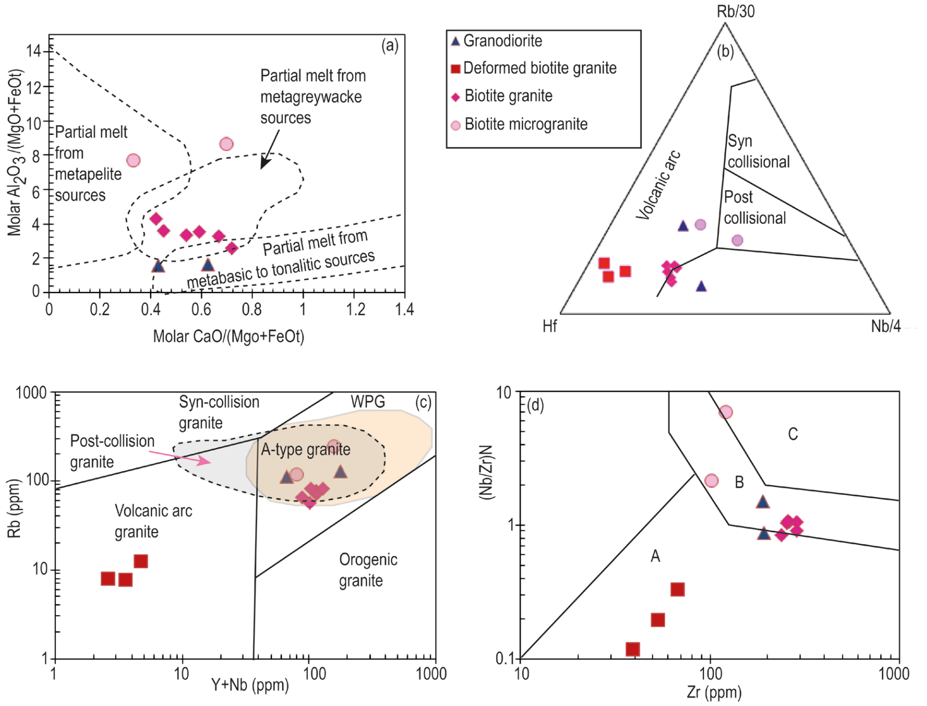

Figure 12. Sources and tectonic discrimionation diagram of the Goueygoudoum-Fianga granitoids: (a) Molar CaO/(MgO + FeOt) vs Al_2O_3/(MgO + FeOt) of [48]; (b) Hf-Rb/30-Ta × 3; (c) Rb vs. Y + Nb and (d) Zr vs. $(Nb/Zr)_N$ [50]. A = subduction-zone magmatic rocks; B = collision zone rocks; C = alkaline intra-plate zone rocks. Normalization to primitive mantle values from [51].

Structural analysis using the ternary Hf-Nb/4-Rb/30 diagram (**Figure 12(b)**) shows that most studied granitoids fall within the volcanic arc granite field. One notable exception is a fine-grained granite sample that plots in the post-collisional granite domain. In the (Y + Nb) vs. Rb diagram (**Figure 12(c)**), granodiorites, biotite granites, and biotite microgranites display characteristics typical of A-type granites, suggesting emplacement in a post-collisional tectonic setting. The $(Nb/Zr)_N$ vs. Zr diagram (**Figure 12(d)**) indicates that biotite granites fall within the subduction-related magmatic field. Overall, granodiorites, biotite granites, and microgranites are compatible with a continental collision magmatic context. However, one microgranite and one granodiorite sample plot in a transitional zone between subduction and collision fields, suggesting mixed geodynamic conditions during their formation. Finally, a fine-grained granite sample shows a transitional signature between collisional and intraplate settings, reflecting a complex tectono-magmatic evolution possibly linked to lithospheric thinning or reactivation processes.

7. Conclusions

The Goueygoudoum-Fianga granitoids comprise four main lithologies: granodiorite, deformed biotite granite, undeformed biotite granite, and biotite microgranite. These petrographic units exhibit textures ranging from coarse porphyritic to fine-grained, with varied mineral assemblages including plagioclase, biotite, and quartz. The granular to microgranular textures and lath-shaped plagioclase morphology confirm their magmatic origin.

Geochemical analysis of major and trace elements allows the distinction of two principal series of granitoids:

- I-type series, represented by the deformed biotite granites, displays a weakly potassic calc-alkaline affinity. These rocks derive from a mixed magma source, reflecting interaction between mantle-derived melts and crustal materials. Their geochemical signature is consistent with a subduction-related origin, typical of volcanic arc granites.
- A-type series, including granodiorites, undeformed biotite granites, and biotite microgranites, is characterized by a calc-alkaline to strongly potassic calc-alkaline affinity. Petrogenetic data suggest an origin linked to partial melting of metagreywackes, métapelites and metabasic to tonalitic. Although these granites reflect an intraplate setting, their composition reveals mantle influence associated with a subduction environment.

The magmatic evolution of these granitoids is primarily dominated by fractional crystallization processes, likely accompanied by crustal contamination during emplacement.

Acknowledgements

This study was conducted as part of the research activities led by the first author. We extend our sincere gratitude to the administrative authorities of Goueygoudoum and Fianga for their valuable collaboration and for authorizing the field campaigns. We also express our deep appreciation to Mr. Che Stephene of Douala for his indispensable technical assistance during sample pulverization. Finally, we thank the team at ALS Geochemistry-Loughrea (Ireland) for their professionalism and commitment, which enabled the completion of geochemical analyses.

Conflicts of Interest

The authors declare no conflicts of interest regarding the publication of this paper.

References

[1] Hawkesworth, C.J. and Kemp, A.I.S. (2006) Evolution of the Continental Crust. *Nature*, **443**, 811-817. https://doi.org/10.1038/nature05191

[2] Condie, K.C., Belousova, E., Griffin, W.L. and Sircombe, K.N. (2009) Granitoid Events in Space and Time: Constraints from Igneous and Detrital Zircon Age Spectra. *Gondwana Research*, **15**, 228-242. https://doi.org/10.1016/j.gr.2008.06.001

[3] Terentiev, R.A. and Santosh, M. (2018) High Magnesian Granitoids in the Precambrian Continental Crust: Implication for the Continuum between Ferro-Potassic and Magnesio-Potassic Rock Suites. *Lithos*, **314**, 669-682. https://doi.org/10.1016/j.lithos.2018.07.002

[4] Chappell, B.W. and White, A.J.R. (1974) Two Contrasting Granite Types. *Pacific Geology*, **8**, 173-174.

[5] White, A.J.R. and Chappell, B.W. (1988) Some Supracrustal (S-Type) Granites of the Lachlan Fold Belt. *Earth and Environmental Science Transactions of the Royal Society of Edinburgh*, **79**, 169-181. https://doi.org/10.1017/s026359330001419x

[6] Zen, E. (1988) Phase Relations of Peraluminous Granitic Rocks and Their Petrogenetic Implications. *Annual Review of Earth and Planetary Sciences*, **16**, 21-51. https://doi.org/10.1146/annurev.ea.16.050188.000321

[7] Chappell, B.W. and White, A.J.R. (2001) Two Contrasting Granite Types: 25 Years Later. *Australian Journal of Earth Sciences*, **48**, 489-499. https://doi.org/10.1046/j.1440-0952.2001.00882.x

[8] Clarke, D.B. (2019) The Origins of Strongly Peraluminous Granitoid Rocks. *The Canadian Mineralogist*, **57**, 529-550. https://doi.org/10.3749/canmin.1800075

[9] Barbarin, B. (1999) A Review of the Relationships between Granitoid Types, Their Origins and Their Geodynamic Environments. *Lithos*, **46**, 605-626. https://doi.org/10.1016/s0024-4937(98)00085-1

[10] Zhang, R., Lu, J., Wang, R., Yang, P., Zhu, J., Yao, Y., *et al.* (2015) Constraints of in Situ Zircon and Cassiterite U-pb, Molybdenite Re-OS and Muscovite 40Ar-39Ar Ages on Multiple Generations of Granitic Magmatism and Related W-Sn Mineralization in the Wangxianling Area, Nanling Range, South China. *Ore Geology Reviews*, **65**, 1021-1042. https://doi.org/10.1016/j.oregeorev.2014.09.021

[11] Pouclet, A., Vidal, M., Doumnang, J.-C., Vicat, J.-P. and Tchameni, R. (2006) Neoproterozoic Crustal Evolution in Southern Chad: Pan-African Ocean Basin Closing, Arc Accretion and Late- to Post-Orogenic Granitic Intrusion. *Journal of African Earth Sciences*, **44**, 543-560. https://doi.org/10.1016/j.jafrearsci.2005.11.019

[12] Isseini, M., André-Mayer, A., Vanderhaeghe, O., Barbey, P. and Deloule, E. (2012) A-type Granites from the Pan-African Orogenic Belt in South-Western Chad Constrained Using Geochemistry, Sr-Nd Isotopes and U-Pb Geochronology. *Lithos*, **153**, 39-52. https://doi.org/10.1016/j.lithos.2012.07.014

[13] Seguem, N., Alexandre, G.A., Klötzli, U., Kepnamou, A.D. and Emmanuel, E.G. (2014) Petrography and Geochemistry of Precambrian Basement Straddling the Cameroon-Chad Border: The Touboro Baïbokoum Area. *International Journal of Geosciences*, **5**, 418-431. https://doi.org/10.4236/ijg.2014.54040

[14] Shellnutt, J.G., Yeh, M., Lee, T., Iizuka, Y., Pham, N.H.T. and Yang, C. (2018) The Origin of Late Ediacaran Post-Collisional Granites near the Chad Lineament, Saharan Metacraton, South-Central Chad. *Lithos*, **304**, 450-467. https://doi.org/10.1016/j.lithos.2018.02.020

[15] Djerossem, F., Berger, J., Vanderhaeghe, O., Isseini, M., Ganne, J. and Zeh, A. (2020) Neoproterozoic Magmatic Evolution of the Southern Ouaddaï Massif (Chad). *BSGF-Earth Sciences Bulletin*, **191**, Article 34. https://doi.org/10.1051/bsgf/2020032

[16] Diontar, M., Doumnang, J.C., Kwékam, M., Al-hadj Hamid, Z., Kagou Dongmo, A., Efon Awoum, J., *et al.* (2020) Petrogenesis of Magnesian High-K Granitoids from Bitkine (Centrechad Massif): Major and Trace Elements Constraints. *European Journal of Environment and Earth Sciences*, **1**, 1-6. https://doi.org/10.24018/ejgeo.2020.1.5.78

[17] Seguem, N., Diondoh, M., Kepnamou, A.D., Mama, N., Sami, M., Alexandre, G.A., *et al.* (2022) Petrography and Geochemistry of Baïbokoum-Touboro-Ngaoundaye Granitoids on the Chad-Cameroon-RCA Borders (Adamawa-Yade Domain). *Open Journal of Geology*, **12**, 136-155. https://doi.org/10.4236/ojg.2022.122007

[18] Assadi, A.O., Emmanuel, N.N. and Fadimatou, Y.N. (2022) Petrogenesis and Tectonic Setting of the Gold-Bearing Magmatic Rocks of the North-Western Melfi Massif, Central Chad. *European Journal of Environment and Earth Sciences*, **3**, 23-31. https://doi.org/10.24018/ejgeo.2022.3.4.304

[19] Castaing, C., Feybesse, J.L., Thiéblemont, D., Triboulet, C. and Chèvremont, P. (1994) Palaeogeographical Reconstructions of the Pan-African/Brasiliano Orogen: Closure of an Oceanic Domain or Intracontinental Convergence between Major Blocks? *Precambrian Research*, **69**, 327-344. https://doi.org/10.1016/0301-9268(94)90095-7

[20] Abdelsalam, M.G., Liégeois, J. and Stern, R.J. (2002) The Saharan Metacraton. *Journal of African Earth Sciences*, **34**, 119-136. https://doi.org/10.1016/s0899-5362(02)00013-1

[21] Isseini, M. (2011) Croissance et différenciation crustales au Néoprotérozoïque: Exemple du domaine panafricain du Mayo Kebbi au Sud-Ouest du Tchad. Thèse de Doctorat, Université Henri Poincaré, Nancy I (France), 342 p.

[22] Abdelsalam, M.G., Gao, S.S. and Liégeois, J. (2011) Upper Mantle Structure of the Saharan Metacraton. *Journal of African Earth Sciences*, **60**, 328-336. https://doi.org/10.1016/j.jafrearsci.2011.03.009

[23] Nesbitt, H.W. and Young, G.M. (1984) Prediction of Some Weathering Trends of Plutonic and Volcanic Rocks Based on Thermodynamic and Kinetic Considerations. *Geochimica et Cosmochimica Acta*, **48**, 1523-1534. https://doi.org/10.1016/0016-7037(84)90408-3

[24] Potter, P.E., Maynard, J.B. and Depetris, P. (2005) Mud and Mudstones Introduction and Overview. Springer Science and Business Media, 296.

[25] Fedo, C.M., Wayne Nesbitt, H. and Young, G.M. (1995) Unraveling the Effects of Potassium Metasomatism in Sedimentary Rocks and Paleosols, with Implications for Paleoweathering Conditions and Provenance. *Geology*, **23**, 921-924. https://doi.org/10.1130/0091-7613(1995)023<0921:uteopm>2.3.co;2

[26] Le Maitre, R.W. (1989) A Classification of Igneous Rocks and Glossary of Terms: Recommendations of the IUGS Subcommission on the Systematics of Igneous Rocks. Blackwell, 130-171.

[27] Chappell, B.W. and White, A.J.R. (1992) I- and S-Type Granites in the Lachlan Fold Belt. *Earth and Environmental Science Transactions of the Royal Society of Edinburgh*, **83**, 1-26. https://doi.org/10.1017/s0263593300007720

[28] Frost, B.R., Barnes, C.G., Collins, W.J., Arculus, R.J., Ellis, D.J. and Frost, C.D. (2001) A Geochemical Classification for Granitic Rocks. *Journal of Petrology*, **42**, 2033-2048. https://doi.org/10.1093/petrology/42.11.2033

[29] Peccerillo, A. and Taylor, S.R. (1976) Geochemistry of Eocene Calc-Alkaline Volcanic Rocks from the Kastamonu Area, Northern Turkey. *Contributions to Mineralogy and Petrology*, **58**, 63-81. https://doi.org/10.1007/bf00384745

[30] Maniar, P.D. and Piccoli, P.M. (1989) Tectonic Discrimination of Granitoids. *Geological Society of America Bulletin*, **101**, 635-643. https://doi.org/10.1130/0016-7606(1989)101<0635:tdog>2.3.co;2

[31] Rickwood, P.C. (1989) Boundary Lines within Petrologic Diagrams Which Use Oxides of Major and Minor Elements. *Lithos*, **22**, 247-263. https://doi.org/10.1016/0024-4937(89)90028-5

[32] Sun, S.-S. and McDonough, W.F. (1989) Chemical and Isotopic Systematics of Oceanic Basalts: Implications for Mantle Composition and Processes. *Geological Society, London, Special Publications*, **42**, 313-345. https://doi.org/10.1144/gsl.sp.1989.042.01.19

[33] Ma, C., She, Z., Xu, P. and Wang, L. (2005) Silurian A-Type Granitoids in the Southern Margin of the Tongbai-Dabieshan: Evidence from SHRIMP Zircon Geochronology and Geochemistry. *Science in China Series D: Earth Sciences*, **48**, 1134-1145. https://doi.org/10.1360/03yd0487

[34] Bonin, B. (2007) A-Type Granites and Related Rocks: Evolution of a Concept, Problems and Prospects. *Lithos*, **97**, 1-29. https://doi.org/10.1016/j.lithos.2006.12.007

[35] Shellnutt, J.G., Denyszyn, S.W. and Pang, K. (2021) Editorial: Granite Petrogenesis and Geodynamics. *Frontiers in Earth Science*, **8**, Article 637729. https://doi.org/10.3389/feart.2020.637729

[36] Penaye, J., Kroner, A., Toteu, S.F., Van Schmus, W.R. and Doumnang, J. (2006) Evolution of the Mayo Kebbi Region as Revealed by Zircon Dating: An Early (ca. 740ma) Pan-African Magmatic Arc in Southwestern Chad. *Journal of African Earth Sciences*, **44**, 530-542. https://doi.org/10.1016/j.jafrearsci.2005.11.018

[37] Whalen, J.B., Currie, K.L. and Chappell, B.W. (1987) A-type Granites: Geochemical Characteristics, Discrimination and Petrogenesis. *Contributions to Mineralogy and Petrology*, **95**, 407-419. https://doi.org/10.1007/bf00402202

[38] Workman, R.K. and Hart, S.R. (2005) Major and Trace Element Composition of the Depleted MORB Mantle (DMM). *Earth and Planetary Science Letters*, **231**, 53-72. https://doi.org/10.1016/j.epsl.2004.12.005

[39] Li, H., Palinkaš, L.A., Watanabe, K. and Xi, X. (2018) Petrogenesis of Jurassic A-Type Granites Associated with Cu-Mo and W-Sn Deposits in the Central Nanling Region, South China: Relation to Mantle Upwelling and Intra-Continental Extension. *Ore Geology Reviews*, **92**, 449-462. https://doi.org/10.1016/j.oregeorev.2017.11.029

[40] Hofmann, C., Courtillot, V., Féraud, G., Rochette, P., Yirgu, G., Ketefo, E., *et al.* (1997) Timing of the Ethiopian Flood Basalt Event and Implications for Plume Birth and Global Change. *Nature*, **389**, 838-841. https://doi.org/10.1038/39853

[41] Condie, K.C. (2005) High Field Strength Element Ratios in Archean Basalts: A Window to Evolving Sources of Mantle Plumes? *Lithos*, **79**, 491-504. https://doi.org/10.1016/j.lithos.2004.09.014

[42] Wilson, W. (1989) Igneous Petrogenesis. Unwin Hyman, 373.

[43] Siégel, C., Bryan, S.E., Allen, C.M. and Gust, D.A. (2018) Use and Abuse of Zircon-Based Thermometers: A Critical Review and a Recommended Approach to Identify

Antecrystic Zircons. *Earth-Science Reviews*, **176**, 87-116. https://doi.org/10.1016/j.earscirev.2017.08.011

[44] Tchameni, R., Pouclet, A., Penaye, J., Ganwa, A.A. and Toteu, S.F. (2006) Petrography and Geochemistry of the Ngaoundéré Pan-African Granitoids in Central North Cameroon: Implications for Their Sources and Geological Setting. *Journal of African Earth Sciences*, **44**, 511-529. https://doi.org/10.1016/j.jafrearsci.2005.11.017

[45] Wu, D., Sun, F., Pan, Z. and Tian, N. (2020) Geochronology, Geochemistry, and Hf Isotopic Compositions of Triassic Igneous Rocks in the Easternmost Segment of the East Kunlun Orogenic Belt, NW China: Implications for Magmatism and Tectonic Evolution. *International Geology Review*, **63**, 1011-1029. https://doi.org/10.1080/00206814.2020.1740895

[46] Moyen, F., Laurent, O., Chelle-Michou, C., Couzinié, S., Vanderhaeghe, O., Zeh, A., *et al.* (2017) Collision Vs. Subduction-Related Magmatism: Two Contrasting Ways of Granite Formation and Implications for Crustal Growth. *Lithos*, **277**, 154-177. https://doi.org/10.1016/j.lithos.2016.09.018

[47] Asaah, A.V., Zoheir, B., Lehmann, B., Frei, D., Burgess, R. and Suh, C.E. (2014) Geochemistry and Geochronology of the ~620 Ma Gold-Associated Batouri Granitoids, Cameroon. *International Geology Review*, **57**, 1485-1509. https://doi.org/10.1080/00206814.2014.951003

[48] Altherr, R., Holl, A., Hegner, E., Langer, C. and Kreuzer, H. (2000) High-Potassium, Calc-Alkaline I-Type Plutonism in the European Variscides: Northern Vosges (France) and Northern Schwarzwald (Germany). *Lithos*, **50**, 51-73. https://doi.org/10.1016/s0024-4937(99)00052-3

[49] Doumnang, J.-C. (2006) La géologie des formations Néoprotérozoïques du Mayo-Kebbi (Sud-Ouest du Tchad). Thèse de Doctorat, Université d'Orléans, 206 p.

[50] Pearce, J.A., Harris, N.B.W. and Tindle, A.G. (1984) Trace Element Discrimination Diagrams for the Tectonic Interpretation of Granitic Rocks. *Journal of Petrology*, **25**, 956-983. https://doi.org/10.1093/petrology/25.4.956

[51] McDonough, W.F. and Sun, S.-S. (1995) The Composition of the Earth. *Chemical Geology*, **120**, 223-253. https://doi.org/10.1016/0009-2541(94)00140-4